Radio Observations at 232 MHz and Multifrequency Spectral Studies of the SNR HB21

Xi-Zhen Zhang[1,2] *, L. A. Higgs[3], T. L. Landecker[3], Xin-Ji Wu[4] and
Shan-Jie Qian[1]

[1] National Astronomical Observatories, Chinese Academy of Sciences, Beijing 100012
[2] The Partner Group of MPIfR at NAO, Chinese Academy of Sciences, Beijing 100012
[3] Dominion Radio Astrophysical Observatory, P. O. Box 248, Penticton, B. C. V2A 6K3, Canada
[4] Department of Astronomy, Peking University, Beijing 100871

Abstract Radio observational results at 232 MHz and multifrequency studies of the supernova remnant (SNR) HB21 are presented. Its integrated flux density at 232 MHz is about 390 ± 30 Jy. Both the integrated spectral index and the spatial variations of spectral index of the remnant were calculated by combining the new map at 232 MHz with previously published maps made at 408, 1420, 2695, and 4750 MHz. The SNR has an integrated spectral index of about $\alpha = -0.43$ ($S_\nu \propto \nu^\alpha$) between 232 and 4750 MHz. In general the spectral index varies from –0.5 in southeast and west regions of the remnant to –0.3 in the central region and near the northwest edge. The new data of 232 MHz reveal that there is interaction between the remnant and the surrounding gas along the east edge of the remnant which causes the spectrum flattening at low frequency, while the very good agreement between the structure of X-ray emission and the central flat spectrum area suggests that the existence of thermal emission is the reason of spectrum flattening in the area.

Key words: ISM: supernova remnants – ISM: structure

1 INTRODUCTION

HB21 (G89.0+4.7) is an evolved supernova remnant having an angular size of about $1.5°$(NS) $\times 2.0°$ (EW). It was discovered by Brown and Hazard (1953) at 159 MHz. Its radio continuum emission has been studied in considerable detail (e.g., Erkes & Dickel 1969; Kundu 1971; Kundu et al. 1973; Hill 1974; Willis 1973; Haslam et al. 1975; Reich et al. 1983). Willis (1973) showed that the source has a spectral index of $\alpha = -0.4$. Weak X-ray emission from the interior of HB21 was observed by Leahy (1987).

---

* E-mail: zxz@ns.bao.ac.cn

The shape of the remnant is not circular, and several results (Erkes & Dickel 1969) suggested that the northern V-shape boundary of the remnant may be due to collision with dense interstellar material (ISM). Also Tatematsu et al. (1990) showed that an interstellar gas wall, consisting of atomic and molecular gas, is thought to have caused the straight eastern boundary of the remnant by impeding the expansion of the blast wave. Willis (1973) found that the spectrum of HB21 is quite straight, while Kundu (1971) gave the conclusion that the spectrum of HB21 may have a bend at about 600 MHz. Willis also reported that the spectrum of the center region of the remnant may be much steeper, while the spectrum becomes flat in the northwest. Erkes and Dickel (1969) reported that there is a curved and flat spectrum in the northern shell and a straight spectrum in the southern shell.

In this paper, new observations with high resolution at 232 MHz are presented. The observations were carried out with the Miyun Synthesis Radio Telescope (MSRT) of the Beijing Astronomical Observatory (Wang 1985). By combining the new data with previously published data of 408 and 1420 MHz (Tatematsu et al. 1990), 2695 and 4750 MHz (Haslam et al. 1975; Reich et al. 1983), the integrated spectra and spectral distribution over HB21 are obtained.

Section 2 describes the observations at 232 MHz and the data reduction. The intensity structure, integrated spectrum, and spatial spectral variations are given in Sections 3.1 and 3.2 respectively. A discussion on the spectra of HB21 is given in Section 4.

2   OBSERVATION AND DATA REDUCTION

2.1   Observation

The observations were carried out with the MSRT in June 1992. The telescope consists of 28 antennas, each 9 m in diameter, on an East-West baseline, providing complete baseline coverage from 18 m to 1164 m. The array is divided into two sub-arrays. Those 16 antennas locating in the central part are the elements of Sub-array A with the same separation of 72 m, the rest 12 antennas, separated by 12 m, standing with six dishes on each side of Sub-array A, constitute Sub-array B. Only three antennas in each side of Sub-array A are used in each observation, resulting in 96 interferometer pairs from the combinations $Ai \times Bj (i = 1, 16, j = 1, 6)$. A two-day observing run gives a complete UV coverage of 192 baselines. Table 1 summarizes the parameters of the observations and the telescope.

Table 1   The Parameters for MSRT

observing frequency	232 MHz
antenna	9 m parabolic
number of antennae	28
primary beam	$10° \times 12°$
baseline	1164 m E-W
spacing interval	6 m
number of baselines	192
min./max. baseline	18/1164 m
synthesis beam	$3.8' \times 3.8' \csc \delta$
trans. frontend noise	100 K (232)
band width	1.5 MHz
sampling interval	10 s
path compensation	digital
correlator	96

Daily calibration (phase and amplitude) relies on frequent observations of the calibrators. Cygnus A is one of the calibrators. It is modelled as a double point source by referring to other frequency data, as it is partly resolved by the longer baselines of MSRT. BGPW flux system (Baars et al. 1973) is used to scale the observational intensity to flux density. Cygnus A is used as the first calibrator for 232 MHz observations. Flux density of Cygnus A is taken as 7944 Jy calculated from Baars's formula. It is used only for correcting the constant

parts of the relative amplitudes and phases of the 96 channels at the observational stage. At this stage the calibration accuracy is about 5° in phase and 10% in amplitude. At the final data

reduction stage, on the map-plane, 3C 418 is used as the secondary calibrator because there are possible gain-variations caused by system AGC between the observations of Cygnus A and HB21. Its flux density at 232 MHz is obtained by a quadratic curve fitting with flux densities of 178 MHz (3CR), 408 MHz (DRAO), and 4850 MHz (87GB). All data adopted for the fitting have been adjusted to the BGPW scale. The fitted flux density is 13.2 Jy.

2.2 Data Reduction

As the working frequency (232 MHz) is low, MSRT data suffer from irregularities of ionosphere and man-made interference. In general 15 percent of the recorded data are rejected. To remove the effects of interference and to compensate for zero-offset error, some correction procedures have been developed. (Yang et al. 1990). The description of reduction of MSRT data in detail can be found in Zhang et al. (1993 and 1997a). After the data-editing mentioned above, the observed data are then sent to AIPS for further self-calibration and map CLEAN. At 232 MHz, ionospheric irregularities can cause source position shift on the scale of tens arcsecond, peak-intensity reduction, and side-lobe rise. Two methods, linear analysis and one dimensional imaging, were used to extract information on ionospheric irregularity (Han et al. 1993; Zheng 1993; Zhang et al. 1990). In the case of large position shift, position-reference-sources taken from Texas catalog (Duglas et al. 1996) were used.

The 408 MHz and 1420 MHz maps from DRAO are added with single dish data for the missing short spacings and the maps of 2695 and 4750 MHz are single dish scans. In the case of MSRT, the short spacings, 0, 1, and $2d_0$ ($d_0 = 6$ m) are missed during the observations and cause a weak negative background, the "big bowl". For large angular objects such as HB21, the decrease of the integrated flux of MSRT data caused by the missing short-spacings is about 20 percent, as obtained by simulating an object two degrees in diameter with the MSRT Array (Zhu 1994). A method has been developed (Zhang 1995) for the compensation of the missing spacings using only interferometer data, following Wakker and Schwarz (1990), and Braun and Walterbos (1985). As we know a CLEAN map can be represented by an equation of the form, [M]=[CC]*[B], where [CC] and [B] are the clean components and beam respectively. The [CC] can be used in calculating new UV-data with an array which has the $1d_0$ and $2d_0$ spacings only. The new UV-data can then be added to the observed UV-data which have no $1d_0$ and $2d_0$ UV-data. The compound UV-data could then be used to make a new CLEAN map for the new [CC]. After several iterations, the "big bowl" is almost invisible.

3 RESULTS

3.1 Radio Morphology of HB21

The intensity map of HB21 at 232 MHz is shown in Fig. 1. The structure agrees very well with that obtained at other frequencies. HB21 shows some of the features of a shell source. The brighter peaks appearing along the inner edge of the source show an obvious shell structure, but the shell near the west boundary of the remnant does not show shell feature as clear as other parts.

The 232 MHz map confirmed some structural features described by Tatematsu (1990) and Hill (1974). For example, only a small fraction of the total flux originates either in the outer ridge or in the central part, as seen in projection. One filament can be seen clearly from the map. It is located at R.A. 20^h45^m, Dec. $50°30'$ and extends $20'$ in length. As it is more bright at 232 MHz, its spectrum must be steeper.
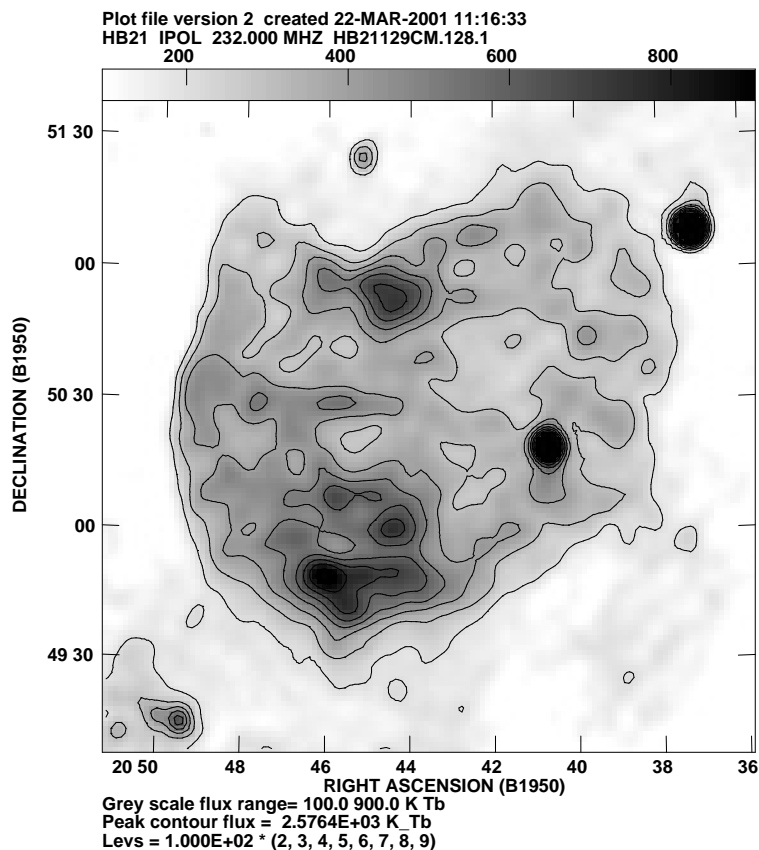
Fig. 1   The intensity map of HB21 observed with the MSRT at 232 MHz.

3.2   Spectrum

Willis (1973) gave an integrated spectral index of -0.40 ± 0.03 of the straight spectrum. He also gave the spectral index variations with a possible error ± 0.2 between 2.7 GHz and 5 GHz. Kundu's result (1971) is that the remnant has a spectral index of –0.48 between 600–5000 MHz with a curvature below 600 MHz. Erkes and Dickel (1969) mentioned that the spectrum of HB21 is relatively straight in the central and southern parts with a mean slope of –0.4, but in the northern shell segment it is curved with a turnover at about 250 MHz. Between 1.4 GHz and 2.7 GHz, Haslam et al. (1975) gave a temperature spectral index $(T \propto \nu^{-\beta})^1$ of 2.8.

In this paper we report the results obtained by combining the new, low frequency data with previously published results. The integrated flux density at 232 MHz of HB21 is about 390 ± 30 Jy, as measured from Fig. 1. By combining this integrated flux density with that measured at 408 MHz (290 ± 20 Jy) and 4750 MHz(110 ± 5 Jy) from the maps of Tatematsu (1990) and Reich (1983), the integrated spectral indices of $-0.41 \pm .02$ and $-0.39 \pm .02$ for frequency pairs of 232–4750 MHz and 408–4750 MHz are obtained respectively. A good linear

---

[1] The corresponding flux density spectral index, $\alpha = 2 - \beta$.

fitting to all the three flux densities can be made. This implies that the integrated spectrum is straight above 232 MHz.

Although these maps are compensated for the missing short spacings, they still have more or less different zero base-levels. Because different base levels can affect the derivation of the integrated flux density of a large angular-size object such as HB21 and HB9, it would be necessary to determine the spectral index by a new way. We use the T-T plot method to derive further the integrated spectral index and spectral variations over the remnant. It was described originally by Costain (1960), and afterwards developed by the staff of DRAO. This method is independent of the base level and is sensitive only to the variation of the temperature of the object. The integrated spectral indices derived by this method are $-0.43 \pm .02$ between 232–4750 MHz and $-0.44 \pm .02$ between of 408–4750 MHz. This also shows that the integrated spectrum of HB21 is straight.

To get the spatial variation of the spectral index, we have developed a method following Anderson and Rudnick (1993). It is an extension of the T–T plot method and is called the *convolution differential-spectral-index* technique. (Zhang 1997b) In this technique, the box for the linear regression analysis is moved across the image in steps of one pixel, and at each position of the box, two values are computed: the slope of the fitted line and the error in the slope. An example of T-T plot is shown in Fig. 2.

One must, however, emphasize the fact that such a method yields the spectral index variation within the analysis box. Thus a weak but spatially varying thermal source, superimposed on a much stronger but non-varying, non-thermal source would produce a thermal spectral index, even though the bulk of the emission at that point is non-thermal. The assessment of the regression errors is important. If the data in a T-T plot are distributed in a long, narrow strip, the regression will give an accurate result (see Fig. 2). However, in a region where variations in brightness temperature are small and are dominated by noise or where both thermal and non-thermal variations are appreciable, the distribution of data would tend to fill a trapezoid and the fitting of a linear regression would be imprecise. In order to estimate the slope and error in the slope of

Fig. 2   An example of the T-T plot method. The slop and error of the fitted line of the pair 232–4750 MHz is 2.48 ± 0.008.

a line of fit in which both X and Y values have errors (either due to noise or a mixture of inherent spectral indices), the regression is done twice, once assuming Y to be a function of X, and once assuming X to be a function of Y. The average slope is then used and the error in the average slope is taken to be one half the difference in the two slopes or the statistical error in the average (based on the formal statistical errors of both fits), whichever is larger.

Spectral spatial variations of HB21 for the frequency intervals 232–4750 MHz, 408–4750 MHz, 232–2695 MHz and 408–2695 MHz have been calculated by this new method. All maps used here were convolved to a resolution of $5.2' \times 4.7'$. The regions where the errors in spectral indices are larger than ± 0.2 are shown as blanks within the remnant. One of these is in a
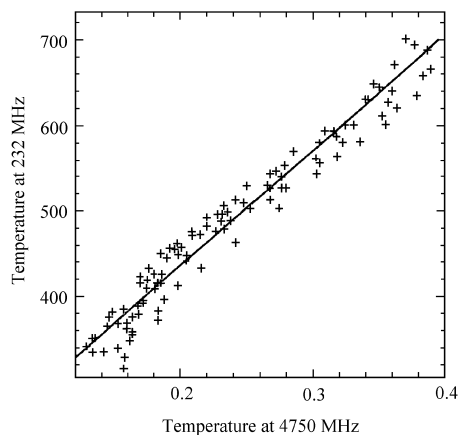
block-shaped region in which the radio source 4C50.52 is located. No calculation was done in this block region.

Figure 3 shows the average map of the four spectral maps mentioned above. It shows almost the same spectral distribution as that obtained from the frequency pair 232–4750 MHz, apart from having a better signal to noise ratio and much smoother variations of spectral indices. To analyze the contribution to the spectral distribution from the low frequency, 232 MHz data, a spectral distribution map using the data of 408, 1420, 2695, and 4750 MHz was obtained with a new method developed by L. Higgs. The result is shown in the Fig. 4. Some common features can be found in Fig. 3 and Fig. 4. They are: 1) the two high intensity regions have steep spectra, 2) flat spectral regions are the central region and northwest edge region. The main difference between the two maps with or without the 232 MHz data occurs at the east of the remnant. The new data of 232 MHz confirmed the conclusion of Tatematsu et al. (1990) that there is interaction along the east edge of the remnant between the remnant and the surrounding gas which causes the spectrum flattening at the low frequency.
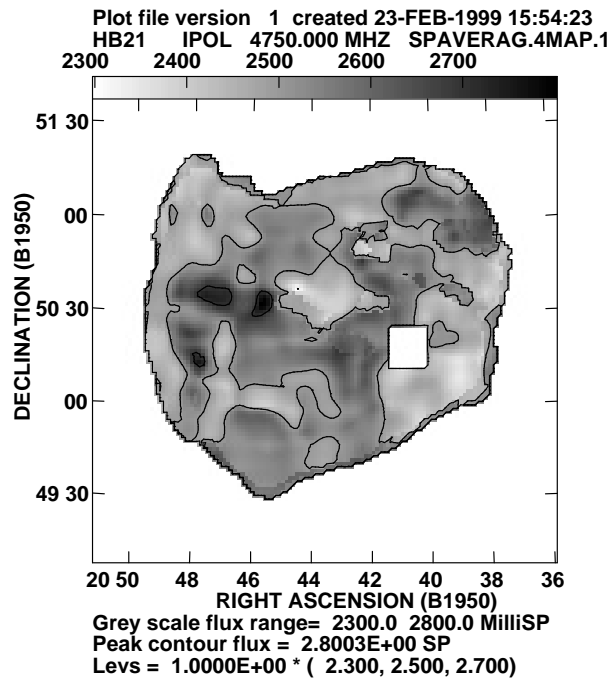

Fig. 3   The frequency-average spectral index map of HB21 using spectral maps of 232–4750 MHz, 408–4750 MHz, 232–2695 MHz, and 408–2695 MHz.

From the spectral maps some results are summarized as follows:

1) The spectral index on scales larger than $10'$ is 2.50 at southeast, falling to 2.35 at northwest, while spectral index is even lower in some regions including the central area of the remnant. The small region in which Willis gave a temperature spectral index about $\beta \sim 0.0$ is at the edges of HB21 in the maps they used. It may be caused by a difference between

the positions of the two maps. Except the small region, the tendency of spectral variation we derived is in general agreement with their conclusion.

2) In the central area of the remnant the spectrum is flat. Its temperature spectral index is about 2.3 whereas on average the spectral index of HB21 is about 2.43. This is opposite to some published results. X-ray emission in the central area has also been found from ROSAT data. Figure 5 gives the ROSAT map of this area which has been convolved to $2' \times 2'$ superposed with the spectral counters. A very good agreement between the X-ray emission structure and the radio flat spectral distribution (β various from 2.3 to 2.35), can be easily seen in Fig. 5. This reveals that the existence of thermal emission in this region is responsible for the spectral flattening.

3) The spectra become flat again near the east edge of the remnant (see Fig. 3). According to Landecker et al. (1990) there is a dense CO gas wall surrounding the remnant. Both the spectral flatenning and the straight shape of the remnant along the east rim are probably due to compression of the gas wall.
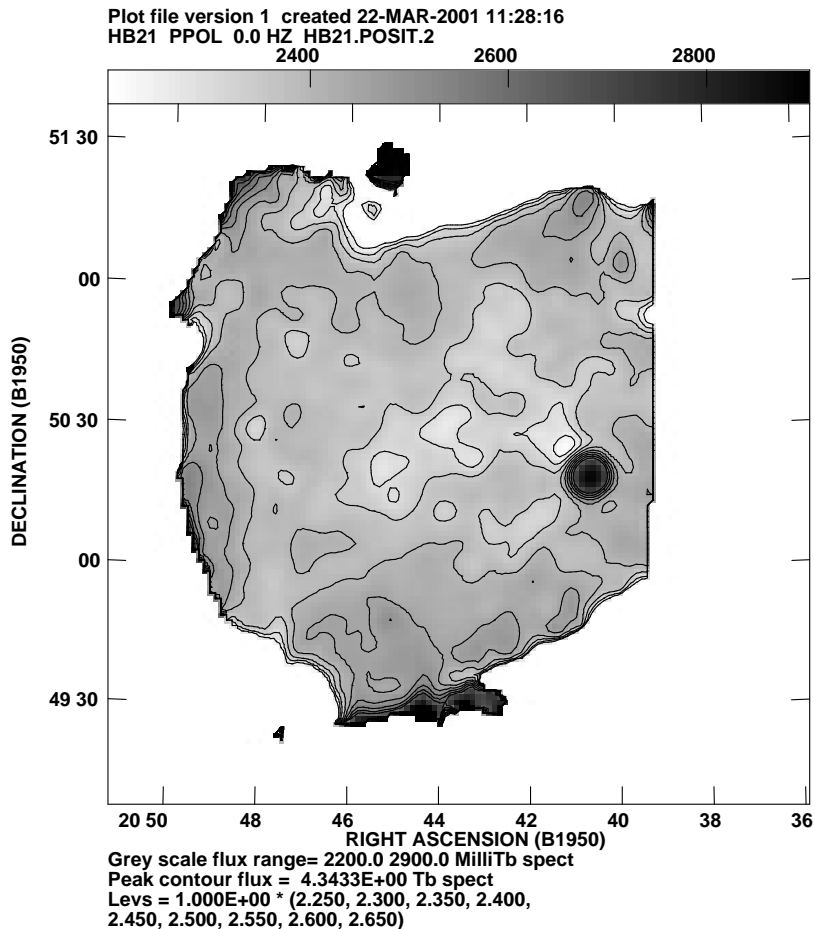

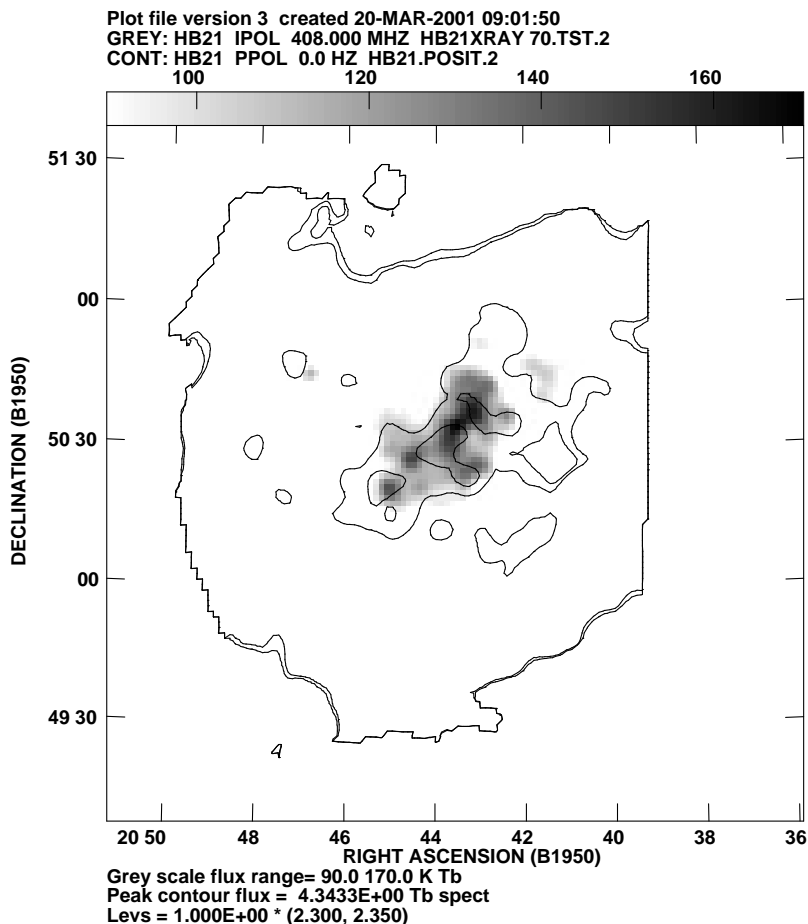Fig. 4   The frequency-average spectral index map of HB21 using the data of 408, 1420, 2695 and 4750 MHz.

Fig. 5   The X-ray map of HB21 taken from the released ROSAT data-base. The X-ray emission region (grey map) is well consistent with the flat spectrum region (contour map) which has temperature spectral index from 2.3–2.35.

4 DISCUSSION

There are several possibilities which can cause spectral variation, for examples: a distribution of relativistic electron energies that varies with position; thermal radio emission; a consequence of compression by interstellar medium, and so on. According to Tatematsu et al. (1990) and Uyaonika et al. (2000), there are HI- and CO- gases along the east and south boundary and HB21 is interacting with the gas. The structure of the central flat spectrum region does not coincide with the optical filaments, but is in good agreement with the structure of X-ray (Leahy 1987; ROSAT data). This phenomenon may be caused by post-shock reheating of the interstellar medium. Since HB21 is an evolved SNR, the ISM in the post-shock region can be reheated up to 10^7 K, so that X-ray from the hot plasma and thermal radio emission could be radiated from this region.

The Galactic background emission is probably another reason which is responsible for the large-scale spectral variation from the southeast to the northwest of HB21, as the direction, along which the spectral index decreases, is nearly in the direction of increasing Galactic latitude. Milne (1987) showed that HB21 has a magnetic field sweeping across the remnant from the north-east to the south-west. This may suggest that the distribution of electrons may be responsible for the coincidence between the Galactic background emission and the spectral variations across the remnant.

The phenomenon of spectral flattening near the east rim obtained from our new result at low frequency is similar to that from SNR HB9 (Leahy et al. 1998). Both HB9 and HB21 are old and evolved supernova remnants. The electron density integrated along the line-of-sight is the highest (Leahy et al. 1998) inside the rim. So absorption by the thermal electrons will be strong there. This causes spectral flattening at low frequency. This is probably one explanation for the spectral spatial distribution obtained by the low frequency observation.

Willis (1973) gave his result of some steep spectral indices appearing in the central area of HB21 which coincides with the optical feature. However, our result shows that no steep spectral index is found in the central area. A very high temperature spectral index of 2.8 between 1.4 GHz and 2.7 GHz was given by Haslam (1975). We checked this result with the addition of the 4.75 GHz flux and found that the $\beta_{1.4}^{2.7}$ and $\beta_{2.7}^{4.75}$ are 2.75 and 1.5, respectively. This means the temperature at 2.7 GHz used here may be too low by a factor of about 1.5. The 178 MHz data (Crother 1965) is the only evidence for the bent spectrum in Erkes and Dickel (1969). But one can find that the 178 MHz flux density has a big error-bar.

5 CONCLUSIONS

Our results show that there are spectral variations over the remnant but no curved spectrum above 232 MHz for the integrated spectrum. The straight integrated spectrum index is about -0.43 in the frequency range from 232–4750 MHz. The flat spectrum regions (α varying from -0.3 to -0.35) are found in the central area and near the northwest edge of HB21, while the steep spectrum areas (α: -0.4 to -0.5) almost agree with the two high intensity areas.

HB21 shows self-absorption at low frequency near the east edge which causes spectrum flattening at 232 MHz while it shows no serious absorption at high frequency. This phenomenon is also found in the study of HB9 (Leahy et al. 1998). Variable thermal electron density near the rim is probably responsible for the spectrum flattening. The difference between HB21 and HB9 is that there is an external compression from the gas wall in the case of HB21 while it is probably an internal compression near the rims of HB9.

References

Anderson M. C., Rudnick L., 1993, ApJ, 408, 514

Baars J. W. M., Genzel R., Pauliny-Toth I. I. K., Witzel A., 1977, A&A, 61, 99

Braun R., Walterbos R. A. M., 1985, A&A, 143, 307

Brown R. H., Hazard C., 1953, MNRAS, 113, 123

Costain C. H., 1960, MNRAS, 120, 248

Crowther J. H., 1965, The Observatory, 85, 110

Duglas J. N. et al., 1996, AJ, 111, 1945

Erkes J. W., Dickel R., 1969, AJ, 74, 840

Fukui Y., Tatematsu K., 1988, IAU Colloquium 101, p.261

Haslam C. G. T., Keen N. J., Wilson W. E. et al., 1975, A&A, 39, 453

Hill I. E., 1974, MNRAS, 169, 59

Han W. J., Zhang X. Z., Zheng Y. J., 1993, in Proceedings of International Symp. on Radio Propagation, p.30

Kundu M. R., 1971, ApJ, 165, L55

Kundu M. R., Bcker R. H., Velusamy T., 1973, AJ, 78, 170

Leahy D. A., 1987, MNRAS, 228, 907

Leahy D. A., Zhang X. Z., Wu X. J. et al., 1998, A&A, 369, 610

Milne D. K., 1987, Aust. J. Phys., 40, 771

Minknowski R., 1958, Rev. Mod. Phys., 30, 1048

Reich W., Furst E., Sieber W., 1983, IAU Symposium 101, 377

Tatematsu K., Fukui Y., Landecker T. L. et al., 1990, A&A, 237, 189

Wakker B. P., Schwarz U. J., 1990, A&A, 200, 312

Wang S. G., 1987, Publications of Beijing Astronomical Observatory, 1

Willis A. G., 1973, A&A, 26, 237

Yang Y. P., Zheng Y. J., Zhang X. Z. et al., 1990, In: J. E. Baldwin, Wang S. G. eds., Proceedings of URSI/IAU Symp. on Radio Astronomical Seeing, p.249

Zhang X., Han Wenjun, Zheng Yijia, 1990, In: J. E. Baldwin, Wang S. G. eds., Proceedings of URSI/IAU Symp. on Radio Astronomical Seeing, p.184

Zhang X., 1995, Annals of Shanghai Observatory, 291

Zhang X., Zheng Y., Chen H. et al., 1993, A&A, 99, 545

Zhang X., Zheng Y., Chen H. et al., 1997a, A&AS, 121, 59

Zhang X., Zheng Y., Landecker T. et al., 1997b, A&A, 324, 641

Zheng Y. J., Han W. J., 1993, In: Proceedings of 1993 International Symp. on Radio Propagation, p.338

Zhu Jian, 1994, in thesis, p.23